Revealing fast Cu-ion transport and enhanced conductivity at the $CuInP_2S_6$ - $In_{4/3}P_2S_6$ heterointerface

Marti Checa[1*], Xin Jin[2,3], Ruben Millan-Solsona[4,5] Sabine. M. Neumayer[1], Michael A. Susner[6], Michael A. McGuire[7], Andrew O'Hara[2], Gabriel Gomila[4,5], Petro Maksymovych[1], Sokrates T. Pantelides[2,8], Liam Collins[1*]

[1]Center for Nanophase Materials Sciences, Oak Ridge National Laboratory, Oak Ridge, Tennessee 37831, USA.

[2]Department of Physics and Astronomy, Vanderbilt University, Nashville, TN 37235, USA.

[3]Institute of Physics & University of the Chinese Academy of Sciences, Chinese Academy of Sciences, Beijing 100190, China.

[4]Institut de Bioenginyeria de Catalunya (IBEC), The Barcelona Institute of Science and Technology (BIST), c/Baldiri i Reixac 11-15, 08028 Barcelona, Spain.

[5]Departament d'Enginyeria Electrònica i Biomèdica, Universitat de Barcelona, Martí i Franqués 1, 08028, Barcelona, Spain.

[6]Materials and Manufacturing Directorate, Air Force Research Laboratory, Wright-Patterson Air Force Base, Ohio 45433, USA.

[7]Materials Science and Technology Division, Oak Ridge National Laboratory, Oak Ridge, Tennessee 37831, USA.

[8]Department of Electrical and Computer Engineering, Vanderbilt University, Nashville, TN 37235, USA.

email: checam@ornl.gov, collinslf@ornl.gov

Abstract

Van der Waals layered ferroelectrics, such as $CuInP_2S_6$ (CIPS), offer a versatile platform for miniaturization of ferroelectric device technology. Control of the targeted composition and kinetics of CIPS synthesis, enables the formation of stable self-assembled heterostructures of ferroelectric CIPS and non-ferroelectric $In_{4/3}P_2S_6$ (IPS). Here, we use advanced quantitative scanning probe microscopy and density-functional-theory to explore in detail the nanoscale variability in dynamic functional properties of the CIPS-IPS heterostructure. We report evidence of fast ionic transport mediating an appreciable out-of-plane electromechanical response of CIPS in the paraelectric phase. Further, we map the local dielectric constant and ionic conductivity on the nanoscale as we thermally stimulate the ferroelectric-paraelectric phase transition, recovering the bulk dielectric peak of the transition at the nanoscale. Finally, we discover a conductivity enhancement at the CIPS/IPS interface, indicating the possibility of engineering its interfacial properties for next generation device applications.

Keywords: copper indium thiophosphate, ionic conductor, ferroelectrics, phase transition, piezoresponse force microscopy, scanning dielectric microscopy

Introduction

Van der Waals (vdW) layered ferroelectrics[1], have the potential to enrich our understanding of ferroelectric physics and polarization stability in the ultrathin regime[2-4] and are also emerging as interesting ferroelectric device candidates due to the favorable interplay of multiple intrinsic properties involving, ionic, electronic, optical, and thermal phenomena[1, 4, 5]. In particular, ionic transport in metal thiophosphates (MTPs) has gained huge attention for applications involving memristors[6], ion-gated synaptic transistors[6], electrochemical energy storage[4] or neuromorphic computing[7]. A material of major interest is $CuInP_2S_6$ (CIPS), a layered, vdW material that features both ionic conductivity and room-temperature ferroelectricity (and under certain conditions antiferroelectricity[8]). CIPS undergoes a first-order, order-disorder transition to a paraelectric phase at T_C ~315 K[9] having a corresponding peak in dielectric properties[2, 10]. Both ionic conductivity and ferroelectricity arise from motion of the Cu ions in the direction perpendicular to the atomic planes. It was recently found that CIPS features a quadruple potential well that corresponds to two low-polarization (LP) and two high-polarization (HP) states, with the Cu ions in planes just below the layer surfaces and just outside the layer surfaces, respectively[11]. The four polarization states manifest as nanometric ferroelectric domains and polarization switching has been observed, with the Cu ions displacing across the layers[11] and across the vdW gaps, which feature the unusual phenomenon of the polarization aligning against the applied electric field[12]. It has been reported that CIPS exhibits DC ionic conductivity and leads to a measurable conduction current[13] and local volume expansion[14].

When synthetized with Cu deficiencies, a dielectric and non-ferroelectric Cu-free phase (IPS) forms and exerts a chemical pressure over the CIPS domains, due to the arrangement of In^{3+} ions and vacant sites in the octahedral network leading to an increase in the CIPS T_C (up to ~335 K)[15-17]. Previous works have demonstrated the possibility to tune CIPS/IPS heterostructures through control of chemical phase separation[14]. Thermal cycling[15] has been shown to be a control parameter for forming, destroying, and reforming intralayer heterostructures to engineer and optimize specific ferroic device structures. The complexity of the spontaneously formed hetero-epitaxial CIPS/IPS composite crystals, along with the possibility to precisely tailor the composite crystals, brings us a rich landscape where hetero-interfacial strain, domain size or T_C, can be tailored for specific applications. Indeed, the complex hierarchical domain structure and the abundance of the domain and phase boundaries may host emergent functionalities and potential topological structures, which have not been deeply studied yet. These naturally formed heterostructures can exist at nanoscale thickness, which is ideal for 2D electronic[18], optoelectronic[19], electrocatalytic[20] and neuromorphic[7] devices.

At the same time, very little is known about the functional properties of the heterostructures during the thermal cycling and the CIPS/IPS in-plane interfaces that naturally emerge in this material system. Questions remain surrounding the mechanism of ion transport in this class of materials, as well as its role in mediating the piezoelectric/electromechanical response. In addition, very little is known about the properties of the heterointerface or how they are modified during phase transitions. To answer such complex questions, multimodal probing of relevant order parameters such as piezoresponse, polarization and conductivity, at the appropriate length scales is necessary.

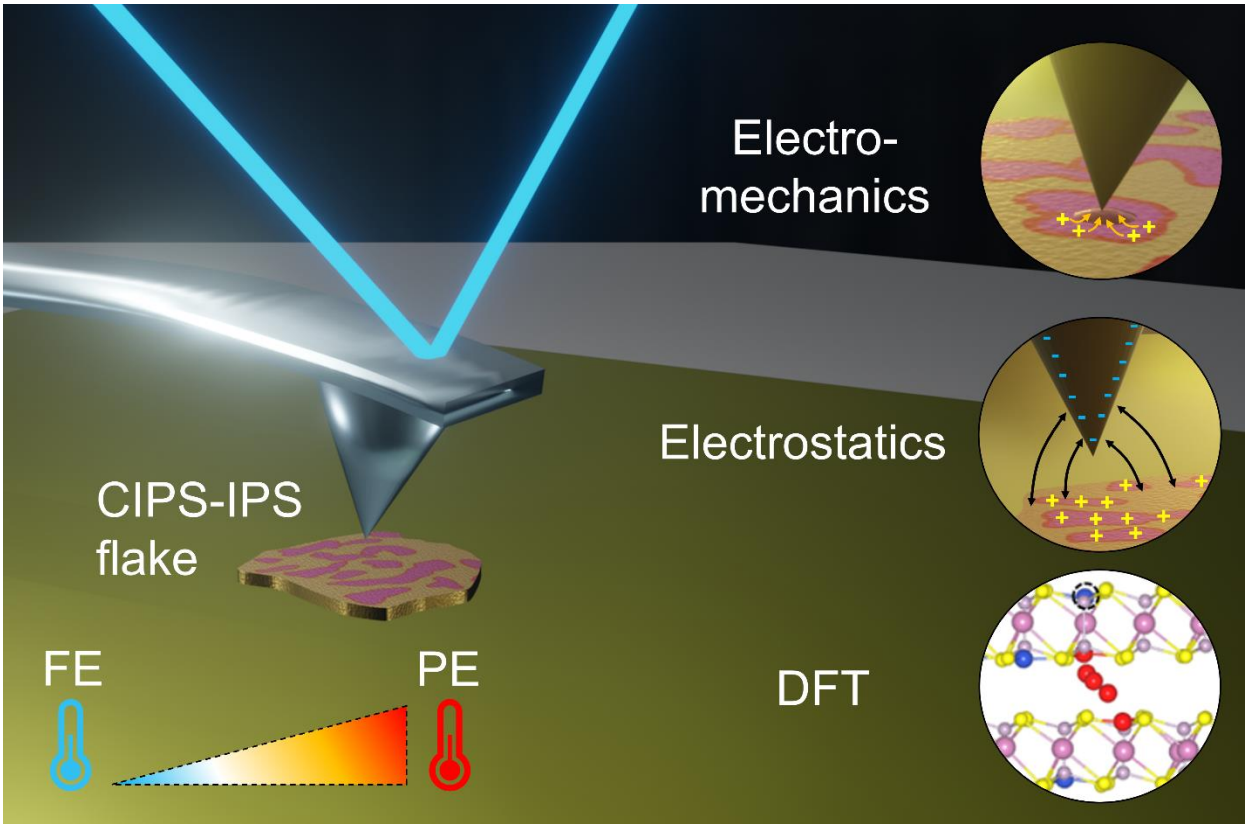

Figure 1: *Quantitative nanoscale imaging of CIPS/IPS flakes.* Simple schematic of the multimodal and correlative nanoscale imaging approach used to map the functional properties across CIPS/IPS heterostructures. Quantitative PFM is used to map the nanoscale electrochemical coupling (piezoresponse and electrochemical strain). SDM is used to quantify its nano dielectric and conductive properties. Finally, DFT simulations are used to interpret the experimental data which is acquired along the thermally stimulated ferrielectric to paraelectric phase transition of the material.

In this work, we use a combination of advanced scanning probe microscopy methods to achieve accurate correlative and quantitative imaging of these order parameters on the nanoscale during the ferrielectric-to-paraelectric phase transition (**Figure 1**). Our results reveal an AC (kHz) ionic contribution to the electromechanical behavior in the CIPS phase. We isolate this effect from the piezoelectric contributions by performing quantitative PFM[21] above the paraelectric transition. Furthermore, we map the dielectric and conductive nanoscale heterogeneities across the ferrielectric-paraelectric transition, imaging the nanoscale dielectric peak in the ferroelectric phase during the first-order phase transition and revealing a heterogeneous and thermally tunable

conductivity of the CIPS/IPS interface. This observed enhancement in interfacial ionic conductivity is accounted for by density-functional-theory (DFT) calculations of the CIPS/IPS heterointerface which reveals that the presence of IPS in a graded interface leads to a lowering of the energy barrier for Cu atoms jumping across vdW gaps on the IPS side. The dielectric peak in CIPS across the ferrielectric-paraelectric phase transition is attributed to large polarization fluctuations[22], the analog of large magnetization fluctuations in ferromagnetic-paramagnetic phase transitions. Therefore, our findings provide a deeper understanding of the relevant nanoscale features governing CIPS/IPS multifunctionally and thus serve as a guide for the nanoscale tunability and functionalization of CIPS/IPS heteroepitaxial structures.

RESULTS AND DISCUSSION

Quantitative PFM: electromechanical response in the paraelectric phase

The most prominent feature of CIPS is the room-temperature ferroelectricity which, in CIPS/IPS composites, is translated into nanostructured electromechanically active and non-active regions, that can be mapped through PFM. Such regions have been correlated in the past with the CIPS/IPS chemical phase separation through various characterization techniques (TEM[23, 24], XRD[15], Raman[17] etc.,). In **Figure 2**, we show the quantitative nanoscale electromechanical characterization by means of interferometric displacement sensing piezoresponse force microscopy[21, 25] (IDS-PFM) of a flat ≈ 170 nm thick CIPS/IPS flake (Figure 2a and b) transferred onto a gold substrate by the scotch-tape transfer method[26]. IDS-PFM measurements were performed across a wide temperature range that goes from 30ºC to 90ºC, showing a transition temperature (T_C) at around 60 ºC.

Below T_C, the Cu-rich CIPS domains exhibit multistate piezoelectricity[11], which we can observe as yellow regions in Figure 2a. A broad distribution of d_{eff} (ranging from 5 pm/V to 12 pm/V) is found, which we attribute to either 1) complex 3D domain structure inside the flake[8], 2) different polarization states present in the material (LP, HP)[11], 3) distinct local strains[27], 4) thickness size-effect[28], or 5) ionic strain, which we will show in more depth below. In our analysis, we fit a single Gaussian curve to the histogram of counts of each image, separating the CIPS response using a mask. Therefore, we find for each temperature an effective piezoelectric constant, $d_{eff,} = \mu \pm \sigma$ pm/V (Figure 2e). Near T_C (~60-70ºC), the piezoelectric coupling reduces drastically (due to the loss of ferroelectricity) showing a quasi-uniform distribution of d_{eff} across the entirety of the flake. In addition, the 180-degree phase contrast, which is present at low temperatures, is no longer present. Finally, above T_C (~80-90ºC) we detect the emergence of a weak AC electromechanical strain of ~1.5pm/V and uniform PFM phase. Since at elevated temperatures CIPS is in its paraelectric phase, the observed electromechanical response is most likely due to the collective AC (kHz) ionic motion of Cu cations under the biased tip, resulting in an electrochemically driven surface displacement due to Vegard strains in the material[29, 30]. While, such strains had previously been measured in CIPS/IPS (and other MTPs[31]) using electrochemical strain microscopy (ESM) under the application of DC fields[32] they had not been observed at kHz frequencies, and their magnitude is drastically reduced from hundreds of nanometers to picometers. This in turn does raise the possibility of electro-chemo-ionic strain also contributing to the overall AC electromechanical response below the phase transition. Noteworthy, quantitative measurements of local volume changes by ESM enabled by interferometric detection sensing, allows us to determine the precise magnitude of the surface electromechanical displacement. In this case, while the contribution of the electrochemical strain is small compared to the apparent piezo response at room

temperature, it may not be negligible, and may also add up (together with the different polarization states of the quadruple well) to the unbalance between piezoresponse of different polarization directions and strains[11]. Alternatively, the electrochemical strain effect may only be relevant (or measurable) above a certain critical temperature (and/or is enhanced as temperature is risen, due to enhanced ionic mobility), following an Arrhenius-type temperature dependence, which has already been measured in other mixed ionic-electronic conductors[33]. In any case, these findings indicate once again that ferroelectricity and ionic motion are intrinsically linked into this type of material and cannot be treated as distinctly separate phenomena.

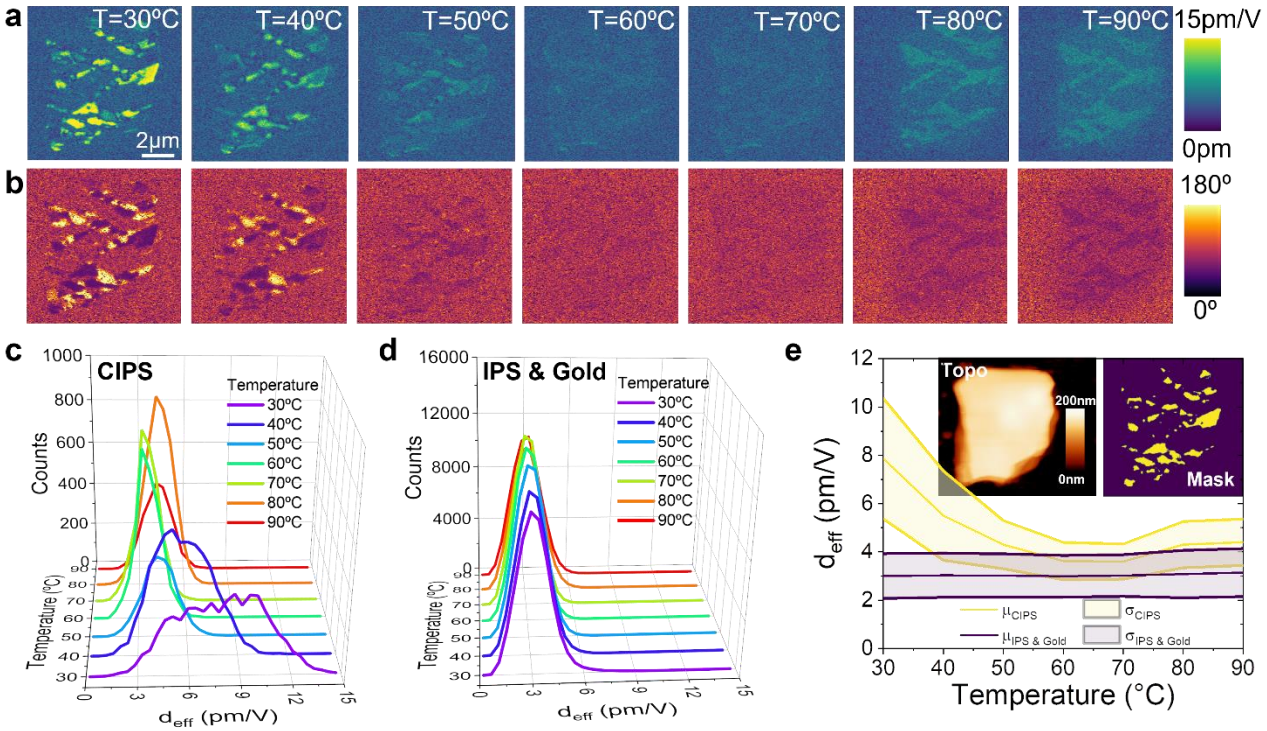

Figure 2: *Quantitative PFM across the phase transition.* a) IDS-PFM Amplitude. b) IDS-PFM Phase. c) Histogram counts for CIPS at different temperatures. d) Histogram counts for IPS and gold at different temperatures. e) d_{eff} for the different phases extracted from the Gaussian fits of data in c) and d). Inset in e) shows the topography of the flake and the mask used for the quantification.

It is important to remember that these conclusions are possible due to the fact that IDS-PFM is free of other spurious electrostatic artifacts and is intrinsically calibrated[34], implying that our

measurements represent true out of plane local surface displacements. Further, our experiment emphasizes the need for techniques complementary to PFM/ESM, for the cases where electromechanical coupling drops drastically until there is no measurable response[11, 35]. Moreover, as ferroelectricity in such complex materials as CIPS/IPS, is directly associated with internal strain, lattice displacements, dielectric behavior, and ionic movement, complementary nanoscopic techniques are needed to fully understand such materials and study them through all the different states of their phase diagram.

Quantitative local dielectric and conductive imaging

The dielectric constant is the key parameter governing how the electric field penetrates inside a material. It indirectly affects the electromechanical coupling present in ferroelectrics and ionic conductors, governing the total deformation under the application of an external electric field. While reliable dielectric bulk characterization can be achieved by means of impedance spectroscopy[36, 37], such measurements lack information on local dielectric properties comprising the different material phases as well as possible inhomogeneities. While scanning probe methods appear well positioned to measure on these length scales, proper dielectric characterization with nanoscale spatial resolution is complicated[38]. Quantification of the real material properties in this way requires a combination of low-noise capacitive detection with local probing and accurate modelling of the tip-sample capacitor to deconvolute the true signal from the measurement artifacts[38]. On the other hand, to obtain a complete nano-electrical picture, the complementary conductive/resistive characterization during the phase transition is also needed. While usually conductivity/resistivity measurements at the nanoscale are performed by conductive AFM (c-AFM), the technique can be invasive[39] (especially in thin ionic conductors like CIPS flakes) inducing topographical changes and/or surface electrochemistry and present additional

complications related to stray capacitances when trying to achieve AC characterization in a broad frequency range.

Scanning Dielectric Microscopy[38] (SDM) measures the out-of-contact local electrostatic forces acting on the tip, when an AC voltage is applied between the conductive tip and a bottom electrode with the sample in between, obtaining the local capacitance gradient and the relative phase of the tip movement with the external excitation (see methods section for details of implementation). SDM has extensively been used to map the dielectric and conductive properties (at the kHz-MHz frequency range) of various types of materials[35, 40-42], under different environmental conditions[43-45]. However, the complex quantification procedure of this technique coupled with its lower sensitivity to high values of dielectric constant[46] (usually the case for most ferroelectrics and ionic conductors), results in SDM not being fully exploited as a technique for the dielectric constant quantification of ferroelectrics[47]. Complementing SDM is Scanning Microwave Microscopy (SMM) which can be utilized to explore dielectric and conductive phenomena on the nanoscale at higher frequencies (GHz) (see Supplementary information S1 for the correlative high-frequency imaging).

In **Figure 3**, we show the SDM imaging and quantification performed at different temperature steps along the phase transition (see the IDS-PFM below and above T_C of that flake in Supplementary Information S3, to identify the CIPS/IPS phase separation). In Figure 3 a-e we present the capacitance gradient images while in Figure 3 f-j we display the 2ω-phase images. These images were taken in two-pass lift-mode using an excitation frequency of 10kHz, at temperatures of 30ºC, 50ºC, 70ºC, 90ºC and 110ºC, respectively (see full dataset with intermediate temperatures in Supplementary material S2). The color scale in the images has been offset by hand so that the gold substrate is always blue to account for changes in the tip-sample capacitor due to

tip wear, lift distance etc. At first sight, from the capacitance gradient images we can clearly distinguish the Cu-rich CIPS regions (white blueish) from the Cu-free IPS regions (red), which is a direct consequence of their difference in dielectric constant. Interestingly, we also observe a defined 2ω-phase contrast, which appears enhanced at the CIPS/IPS interface. Classically[38], such 2ω-phase contrast is attributed to changes in the imaginary part of the dielectric constant or local conductivity/losses of the sample, which we will explore in more depth below.

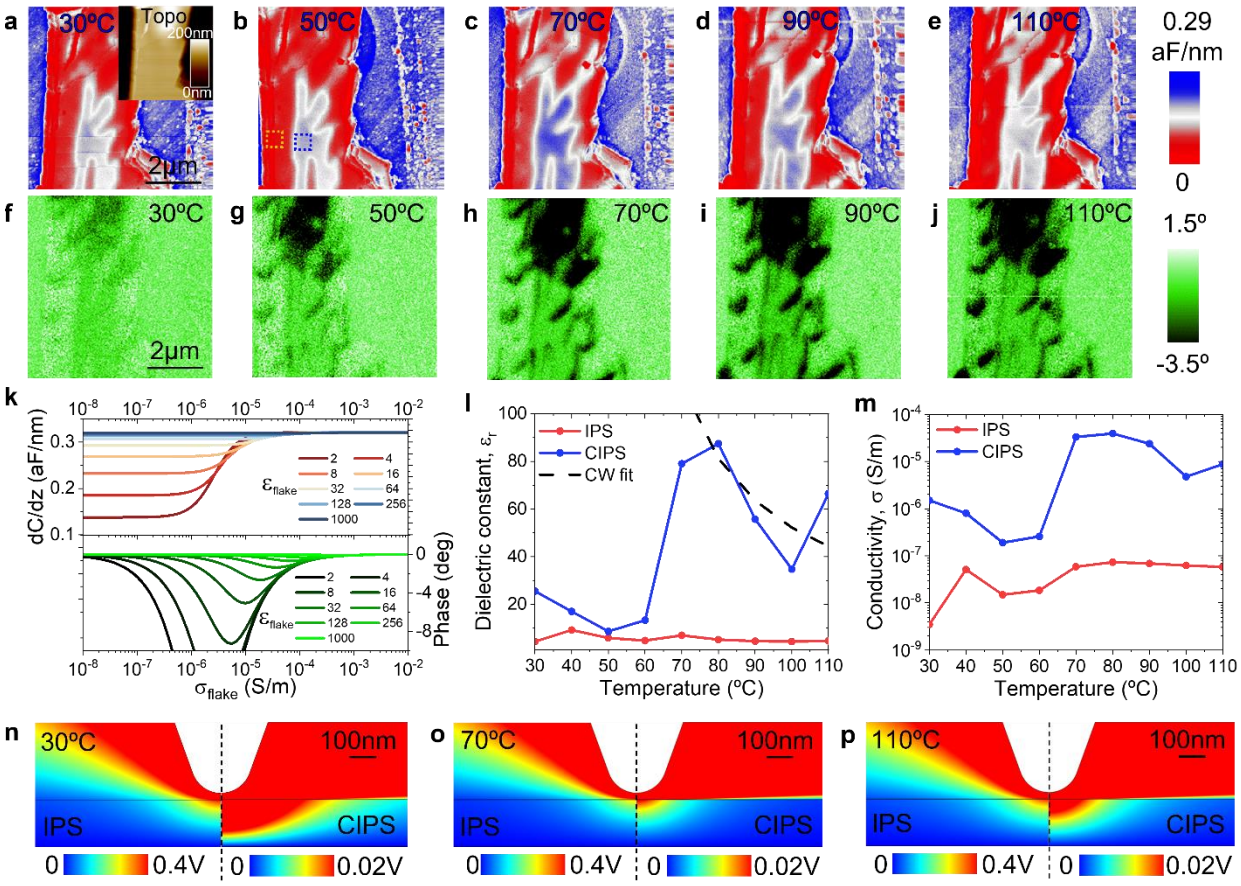

Figure 3: *SDM across the phase transition.* Capacitance gradient (a - e) and 2ω-phase (f - j) images across the phase transition at the temperatures of 30 ºC, 50 ºC, 70 ºC, 90 ºC, 110 ºC. k) Simulated SDM signal dependence upon local dielectric constant and conductivity. l) Local flake dielectric constant as a function of temperature. Black dashed line is the Curie-Weiss fit. m) Local flake conductivity/dielectric loss as a function of temperature. n) Electric potential distribution for IPS (left) and CIPS (right) at T=30 ºC. o) T=70 ºC. p) T=110 ºC.

The temperature dependencies of the SDM signals reveals nanoscale heterogeneities of the dielectric constant and conductivity of the different chemical phases. On the one hand, we clearly observe that the CIPS phase passes from ~0.16aF/nm (white) at low temperature (30ºC), to ~0.21aF/nm (blue) at intermediate temperatures (70ºC) and, finally, back to ~0.18aF/nm (white) at high temperatures (110ºC). Conversely, the IPS regions stay red across the entirety of the temperature range. Qualitatively, these observations indicate that the ferroelectric regions exhibit a dielectric peak when the first-order phase transition takes place, whereas the non-ferroelectric phase does not seem to alter its dielectric properties in this temperature range. On the other hand, we also notice an enhancement of the 2ω-phase contrast found at the CIPS/IPS phase boundaries as temperature is increased, indicating a change of the local resistive properties at this interface which will be explored deeper.

Next, we quantitatively evaluate the SDM images taken at different temperatures. With this aim, finite element simulations are used to correlate the calibrated raw data to the local dielectric constant and conductivity of the sample to account for tip wear, z-lift distance change, etc. The simulations consider a thin-film dielectric and conductive, the details of which can be found in the materials section and elsewhere[46].

In Figure 3k, we simulate the capacitance gradient and 2ω-phase as functions of the local dielectric permittivity and conductivity of the flake for a tip-sample distance of 23.5 nm (matching the experimental tip-sample lift distance). This simulated dataset will be used for quantification of the images to obtain local dielectric constant and conductivity parameters. The simulations show that, for low conductivities ($\sigma_{flake} < 10^{-8}$ S/m), the flake is in "full" dielectric regime and both dC/dz and phase show independent behavior with respect to the conductivity. However, dC/dz shows a high dependence in the dielectric constant ε_{flake}. For high conductivities ($\sigma_{flake} > 10^{-4}$ S/m), the flake is

in the "full" conductive regime, with both dC/dz and phase being independent of both the conductivity and dielectric constant (this being the reason why SDM fails for highly conductive samples). Finally, in the intermediate regime (10^{-8} S/m > σ_{flake} > 10^{-4} S/m), the flake behaves like an insulator with dielectric losses. Here, both dC/dz and phase depend on both dielectric constant and conductivity.

In this intermediate region, the local dielectric permittivity and conductivity can be quantified by fitting the calibrated experimental signals (Figure 3 a-j) to the simulation table (see Supporting information S4 for more details). We performed this procedure for two different regions of the sample, comprising of pure CIPS (blue) and IPS (orange), the location of which are indicated by the dashed square boxes in Figure 3b. Our analysis generates a local dependence of the dielectric constant and conductivity as a function of temperature, shown in Figure 3l and Figure 3m. It is noteworthy that this approach allows us to recover the local nano-electrical fingerprint of each region of the sample with nanometric resolution. We find that, as the temperature rises, the CIPS region experiences its ferrielectric-paraelectric phase transition, indicated by a peak in the dielectric constant centered at T_C. The increase in the dielectric constant below T_C is faster than its decay after T_C, therefore we fit a Curie-Weiss law[48] on the data points above 80ºC (black dashed line in figure 3l), we find a $T_C \sim 317$K, in good agreement with previous works[15]. A more accurate fitting of T_C would require finer temperature steps which is outside of the scope of this work. Conversely, the IPS regions seems to exhibit a rather constant dielectric response across the temperature spectrum. This is in accord with the fact that no phase transition is present in this phase. A similar behavior is also found for the conductivity (or dielectric losses), where the CIPS (contrary to the IPS), experiences an asymmetric peak centered at T_C linked to the higher mobility of Cu ions at higher temperatures. In Figure 3 (n-p), we show the simulated electric potential

distribution used for quantifications, that is generated under the tip during the SDM measurement on top of IPS (left) and CIPS (right) for three different temperatures across the phase transition. As the dielectric constant is approximately an order of magnitude higher for CIPS that for IPS, we set the color scale of the electric potential distribution to be different for each phase, to avoid color saturation.

The appearance of an asymmetric peak in the dielectric constant of CIPS domains as the material goes through a ferroelectric-to-paraelectric phase transition (Fig. 3l) is in accord with similar behavior in the magnetic susceptibility of ferromagnets going through a ferromagnetic-to-paramagnetic phase transition[49]. As noted in the introduction, such a peak has already been observed in bulk CIPS[10, 50] at the respective $T_{C,}$ but never imaged at the nanoscale. The origin of these features is due to the presence of large fluctuations in the order parameter, namely polarization in ferroelectrics. As a base-line reference, we used DFT to calculate the CIPS dielectric tensor ϵ_{ij} as a function of temperature in the absence of large fluctuations. CIPS is an order-disorder ferroelectric and experiments[9] have shown that, if one starts with all the Cu atoms in the -LP polarization state at low temperatures, as the temperature rises, Cu atoms gradually transfer to the +LP sites. As the Curie temperature is reached, the Cu atoms are roughly 50%-50% in the two LP states for a net zero polarization at the Curie temperature. DFT molecular dynamics simulations have indeed confirmed that Cu atoms transfer from the -LP to the +LP sites independently (asynchronously, not synchronously as sheets)[12]. Calculations of the gradual evolution of the polarization based on asynchronous Cu migration have been reported[51]. Along the same lines, we calculated the diagonal elements of the CIPS dielectric tensor using standard perturbation theory for the LP-polarized state, two near-paraelectric states with different Cu arrangements in the ±LP states (see Fig. S5), and a paraelectric ±LP state. We found that ϵ_{ij}

remains roughly constant, with $\epsilon_{xx} = \epsilon_{yy} \approx 9$ and $\epsilon_{zz} \approx 6.7$, in good agreement with the average dielectric constant measured below the Curie temperature (Fig. 3l). Additionally, we calculated the dielectric tensor of IPS. The obtained diagonal components, $\epsilon_{xx} = \epsilon_{yy} \approx 8.3$ and $\epsilon_{zz} \approx 6.5$, are also consistent with the experimental measured value. As the system goes through the Curie temperature, however, polarization fluctuations dominate, and the average dielectric constant is given by [22, 52]:

$$\epsilon = \epsilon_0(\chi + 1)$$

$$\epsilon_0\chi = \frac{\partial P}{\partial E} = \frac{1}{k_B T V}(\langle P^2\rangle - \langle P\rangle^2),$$

where *E* is the electric field and the brackets < > indicate an ensemble average. In 2014, Wojdel and Íñiguez[22] developed a Monte Carlo scheme and computed the evolution of the dielectric constant of the ferroelectric $PbTiO_3$ through the ferroelectric-to-paraelectric phase transition and found a spike very similar to that in Fig. 3l, confirming that such dielectric-constant spikes arise from polarization fluctuations. Such calculations, however, are beyond the scope of this paper.

We also want to remark that our characterization approach shows an alternative (and non-invasive) way of demonstrating ferroelectricity at the nanoscale (especially relevant nowadays with the increased recent interest in 2D ferroelectrics[53, 54] for device miniaturization). Usually, PFM is used to demonstrate ferroelectric coupling in 2D systems[53, 54], but our approach shows that SDM is an elegant alternative to quantify the dielectric constant peak across the thermally stimulated ferrielectric-to-paraelectric phase transition and is not impacted by diminished piezoelectric coefficients or induced surface charges which push measurements below the detection limit of the state-of-the-art PFM techniques.

Enhanced response at CIPS/IPS phase boundary

The high spatial resolution of the technique (of the order of magnitude of the tip radius) allows us to gain insight into how the CIPS/IPS phase boundary itself behaves. Indeed, a distinct behavior takes place right at the CIPS/IPS interface which is not present in both bulk phases (see the zoomed-in images on a CIPS/IPS boundary in Figure 4). Whereas a smooth transition is observed for the capacitance gradient (Figure 4a), a peak is found in the 2ω-phase images, especially noticeable as the temperature increases (Figure 4b).

Unfortunately, the quantification procedure necessary to extract the local dielectric constant and conductivity of the boundary itself is rather complex and requires 3D modelling where information on unknown experimental parameters such as thickness and depth of the chemical phase boundary, 3D hidden domain structure etc. would be needed. Nevertheless, to understand the origin of the qualitative behavior found experimentally, we have simulated the effect that a change in the interfacial conductivity would have in the measured SDM profiles (Figure 4d and S6). To do so, the CIPS/IPS interface has been simulated as a region of width w_i and depth until the end of the material with a certain interfacial dielectric constant ε_{INT} and interfacial conductivity σ_{INT} (which has been ramped from 10^{-8}S/m to 10^{-1}S/m). The corresponding dC/dz and 2ω-phase profiles as the tip scans the sample are calculated for the different $\sigma_{INT,}$ while all the other parameters ($\varepsilon_{CIPS,}$ $\varepsilon_{IPS,}$ ε_{INT}, $\sigma_{CIPS,}$ σ_{IPS}) are fixed to the ones found previously for a specific temperature (we choose the case T=50ºC). For high values of σ_{INT} (>10^{-4}S/m), the corresponding dC/dz profiles experience a peak at the interface that we do not find experimentally, and for low values of σ_{INT} (<10^{-6}S/m), the phase does not experience the peak that we find experimentally. Therefore, we can say that for a mid-range of conductivities 10^{-6}S/m < σ_{INT} <10^{-4}S/m, our simulations match well with the experiments, what would result into an increase in conductivity with respect to σ_{CIPS} and σ_{IPS} found

at this specific temperature of T=50ºC. However, the quantitative values obtained for σ_{INT} can only be valid for an interfacial width of w_i =10nm, and as this parameter is unknown our study is just qualitative. These simulations allow us to prove that an enhanced conductivity at the boundary can reproduce the qualitative behavior that we find experimentally.

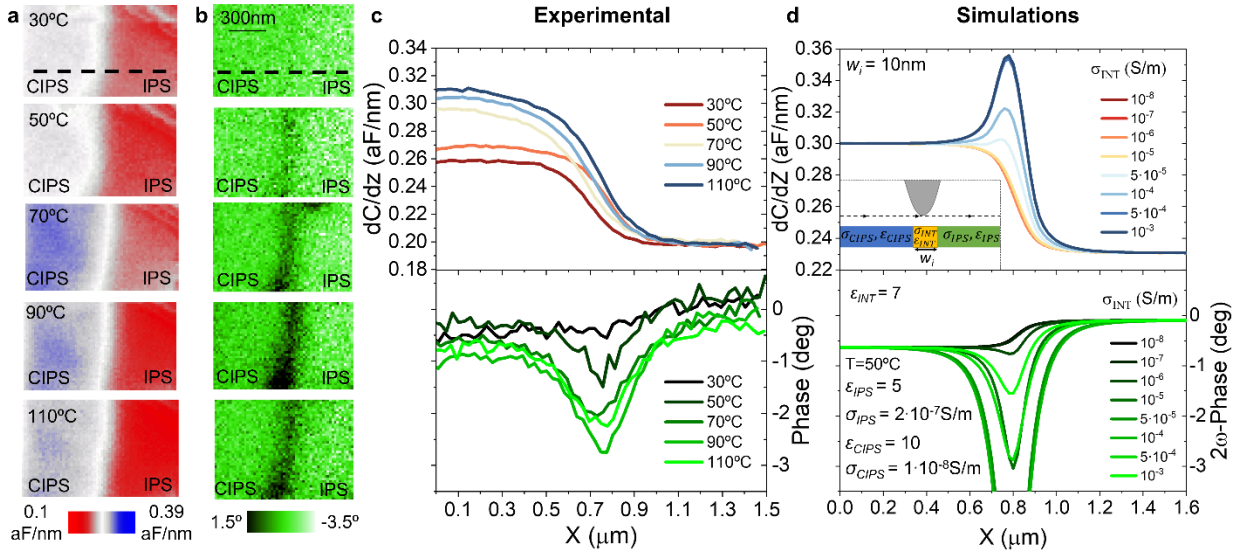

Figure 4: *SDM at the CIPS/IPS phase boundary*. Zoomed in capacitance gradient (a) and 2ω-phase (b) images at the CIPS/IPS phase boundary across the phase transition at the temperatures of 30 ºC, 50 ºC, 70 ºC, 90 ºC, 110 ºC. c) Profiles along the black dashed lines for the different temperatures. Inset shows the full image (same as Figure 3). Dashed yellow rectangle shows the region of the zoom in. d) Finite element model simulations of the CIPS/IPS interface. dC/dZ and 2ω-phase profiles along the CIPS/IPS interface for different phase boundary conductivities (σ_{INT}).

In CIPS/IPS heterostructures like the ones shown in this work, there can be two types of transport: (1) vertical (across the vdW gap) and (2) lateral (within the same vdW layer). Previous works suggest that each mechanism can be differentiated by the timescales that they happen after the application of strong (≈8V) DC pulses[13], while others[55] also claim that in-plane ion migration can generate out-of-plane domain inversion.

To explore the origins of the observed enhanced ionic conductivity at the CIPS/IPS interfaces, we constructed model interfaces and performed pertinent DFT calculations of migration barriers for Cu jumps across the vdW gaps, which are the rate-limiting steps. Calculations of such barriers in pure CIPS were

reported in[12]. The aim of our DFT calculations is not to establish in a unique manner the conduction transport mechanism happening in CIPS, but to explore if the presence of IPS enhances some of the transport pathways for the Cu ions around such type of interfaces, seeking an explanation for the enhanced conductivity we observe at such type of boundaries.

It was found that, in a stoichiometric environment, the energy barrier is ~0.88 eV, while in the presence of Cu vacancies it drops to ~0.84 eV and in the presence of excess Cu atoms it drops to ~0.77 eV. When an electric field equal to -1.0 V/Å is applied, the energy barrier drops to ~0.7 eV.

In constructing CIPS/IPS interfaces, we note that IPS, though often regarded as a Cu-free phase of CIPS, exhibits different structural features from those of CIPS: the PS_6 polyhedral tilting direction with respect to the unit cell, the interlayer stacking order, and the lattice parameters (angle β between lattice vector $\boldsymbol{a}$ and $\boldsymbol{c}$, interlayer distance, etc.) are different for CIPS and IPS, as shown in Fig. S7. We, therefore, constructed three different types of interfaces. In Type 1, we let IPS adopt the CIPS structural features as shown schematically in Fig. S8. In Type 2, we let IPS retain its preferred PS_6 polyhedron tilting direction. In Type 3, we let IPS retain its preferred stacking order. Both Type-1 and Type-2 interfaces are higher-energy configurations relative to the Type-1 interface (Fig. S9).

Using the Type-1 interface, the calculated energy barriers for interfacial Cu atoms at the LP and HP sites in stoichiometric CIPS and in the presence of excess Cu are shown in Fig. 5(a)-(b). They are very similar to the pure CIPS values quoted above[12]. The lowest barrier is ~0.75 eV, which would not result in significant enhancement of the interfacial ionic conductivity. However, the observed CIPS/IPS interfaces are fairly wide, which suggests they are not abrupt but graded. We find that the calculated barrier for a Cu atom in the adjoining IPS region drops to 0.65 eV, as shown in Fig. 5(c). We interpret this result to mean that for Cu atoms that migrate laterally[55] into IPS,

leading to a graded interface, the energy barrier can be reduced by as much as ΔE = 0.1 eV. At room temperature, such lowering of the energy barrier would enhance the conductivity by a factor $e^{\Delta E/k_B T} \sim 55$. For comparison, a Cu atom faces a barrier of 0.5-0.6 eV in freestanding IPS with its preferred structural features (Fig. S10).

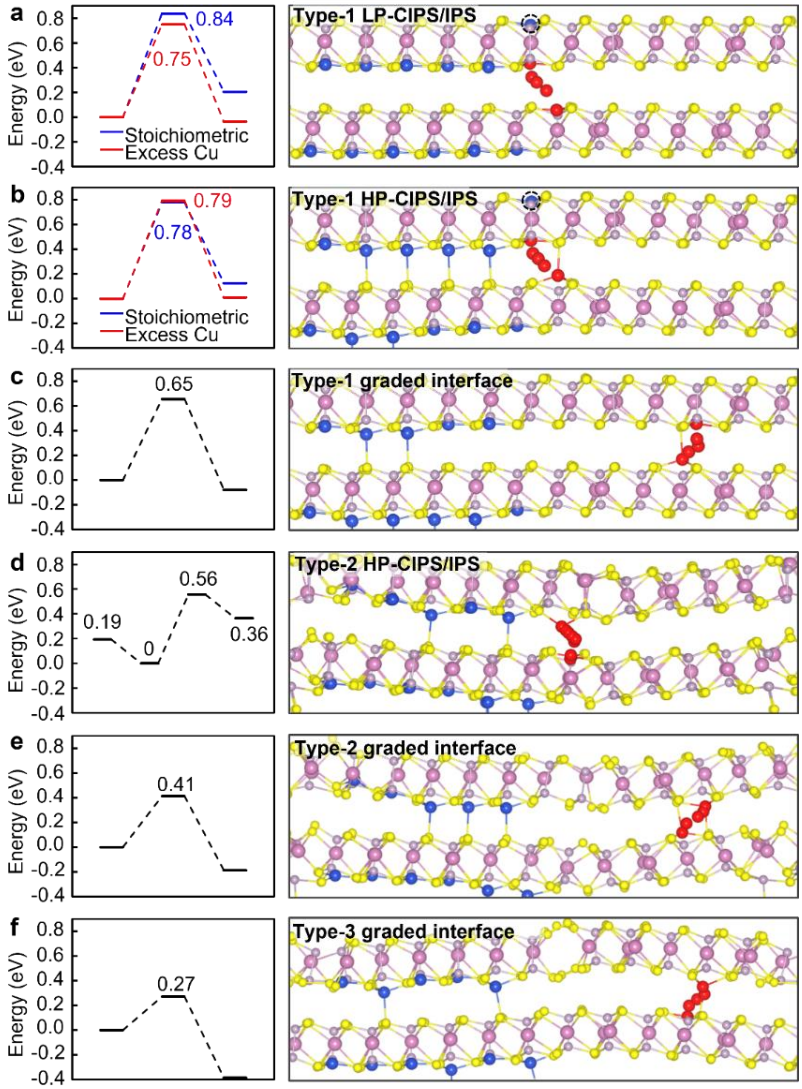

Figure 5: *Density-functional-theory calculations of the CIPS/IPS interphase*. Migration barrier and path of a single Cu atom in different kinds of CIPS/IPS heterostructures. (a)-(c) Cu migration in Type-1 heterostructures: LP-CIPS/IPS, HP-CIPS/IPS and HP-CIPS/IPS with graded interface. (d)-(e) Cu migration in Type-2 HP-CIPS/IPS and HP-CIPS/IPS with graded interface. (f) Cu migration in Type-3 HP-CIPS/IPS with graded interface.

At an abrupt Type-2 interface, the Cu-migration energy barrier is ~0.56 eV (Fig. 5(d)), while at a graded Type-2 interface the barrier can be as small as 0.4 eV (Fig. 5(e)). The enhancement factor can then be as high as three orders of magnitude. Finally, in Type-3, the barriers drop even further (Fig. 5(f)) and would lead to even larger enhancement factors. We note, however, that graded interfaces, which are present in the heterostructures studied here, are inhomogeneous, so that regions with certain average energy barriers are not likely to be continuous throughout the thickness of the material. Thus, the smallest barriers (highest levels of enhancement) are not likely to be observed. Instead, some smaller values are likely to define the rate-limiting step that defines the ionic conductivity. In summary, the DFT calculations of the CIPS/IPS heterointerface find that the presence of IPS in a graded interface indeed leads to a lowering of the energy barrier for Cu atoms jumping across vdW gaps on the IPS side, accounting for the observed enhanced interfacial ionic conductivity which promotes chemical boundary functionalization, increasing nanoscale tunablity of the material towards device implementation.

CONCLUSIONS:

We have used advanced scanning probe microscopy techniques to unravel additional ionic motion tunability in CIPS/IPS thin flakes across the materials thermally stimulated phase transition. First, we used quantitative electromechanical characterization to obtain an artifact-free value of d_{eff} and found evidence of a small electromechanical ionic strain contribution measured above T_C. Additionally, we have used SDM to quantify in a non-invasive manner the nanoscale dielectric constant and ionic conductivity changes across the phase transition and find that, while CIPS exhibits a peak in the dielectric permittivity linked to its phase transition, the IPS phase does not exhibit a peak as it does not undergo a phase transition. Interestingly, there appears to be a temperature-dependent enhanced conductivity at the CIPS/IPS chemical boundaries, that is also

linked to ionic motion. DFT calculations of the CIPS/IPS heterointerface find that the presence of IPS in a graded interface indeed leads to a lowering of the energy barrier for Cu atoms jumping across vdW gaps on the IPS side, accounting for the observed enhanced interfacial ionic conductivity. Our findings provide a deep understanding of the relevant nanoscale features ruling CIPS/IPS multifunctionalities and thus serve as a guide for the nanoscale tunability and functionalization of CIPS/IPS heteroepitaxial structures, especially enticing option for device miniaturization.

METHODS:

Sample preparation:

The sample is composed of exfoliated flakes of CIPS-IPS, transferred directly onto a gold substrate with the scotch tape transfer method[26]. The gold substrate was glued to a commercial atomic force microscopy steel disk and put on a commercial temperature control stage which allows for control and monitoring of the sample temperature.

Piezoresponse force microscopy:

The IDS-PFM used in this study combines a commercial Cypher AFM (Asylum Research, Santa Barbara, CA, USA) with an integrated quantitative laser Doppler vibrometer (LDV) system (Polytec GmbH, Waldbronn, Germany) to achieve highly sensitive electromechanical imaging and spectroscopy. We used Multi75E-G cantilevers with a conductive coating and a nominal spring constant of ~ 3 N/m and free resonance frequency of ~ 75 kHz. The use of interferometric detection allows one to measure the realistic tip displacement whereas the standard OBD detection method measures the angle change of the cantilever (making it hard to deconvolute the true sample

displacement from the cantilever electrostatics). We applied an ac voltage of amplitude 1 V or 1.5 V (depending on the image) at 23kHz.

Scanning Dielectric Microscopy:

We performed SDM measurements in force detection mode using G-Mode EFM approach by means of a custom made Labview/Matlab script, synchronized with a commercial Cypher S AFM system from Asylum Research implemented in PXI architecture using National Instruments NI-6124 fast AWG and DAQcards as described earlier[35]. We used Budget Sensors Multi75E-G conductive probes (Nanosensors) with a spring constant k∼3 N m^{-1}, determined by the manufacturer according to the probe dimensions, resonance frequency f_r∼75 kHz and nominal tip radius R∼10 nm. An ac voltage of amplitude V_{AC} ∼3 V and frequency ω_{EFM} ∼10 kHz, much smaller than the resonance frequency of the cantilever, was applied between the probe and the conducting substrate. The amplitude, $A_{2\omega}$, and phase, $\varphi_{2\omega}$, of the oscillation 2ω harmonic are obtained from the G-mode data stream by digital postprocessing. The conversion of the raw $A_{2\omega}$ data to capacitance gradient values C' was done using the relation:

$$C_z'(aF/nm) = \frac{4k(nN/nm)}{{V_{AC}}^2} \frac{A_{2\omega}(V)}{m\,(V/nm)}$$

where, k is the nominal cantilever spring constant, m the cantilever sensitivity, V_{AC}, the amplitude of the applied excitation and $A_{2\omega}$ the amplitude of the measured response at $2\omega_{EFM}$. The measurements were performed in ambient air at 30% relative humidity.

Modelling and quantification of the dielectric constant and conductivity:

For quantification of the local electric properties of the flake (ε_{flake} and σ_{flake}), we used a finite element numerical model of a thin film of thickness equal to the topography of the measured flake,

with variable dielectric constant and conductivity of the film, implemented in COMSOL Multiphysics 5.6[56]. The tip geometry calibration (tip radius, half cone angle and capacitance gradient offset) was determined by fitting an experimental the capacitance gradient force distance curve measured on the bare part of the metallic gold substrate. This procedure was repeated for each new temperature (to correct for possible tip wearing during the experiment). The quantitative extraction of the local equivalent homogeneous dielectric constant and conductivity of the different sample regions was performed using an algorithm implemented in MATLAB in communication with the COMSOL thin film model. By fitting the acquired experimental signal at each temperature minimizing the error of both capacitance gradient and phase, between the experimental and theoretical simulated theoretical values where the dielectric constant and the conductivity of the thin film model were swept (see Supplementary material S4).

Density Functional Theory calculations

DFT calculations were performed using the Vienna ab initio simulation package (VASP)[57-59] with the projected augmented wave (PAW)[60, 61] method. The exchange-correlation functional for the electrons was described via the generalized gradient approximation in the Perdew-Burke-Ernzerhof (PBE)[62] form. The van der Waals interactions were described by the DFT-D3 (Becke-Jonson (BJ)) method[63-65] as suggested in Ref.[11]. The plane-wave energy cutoff was set as 400 eV for all the calculations. For the structure relaxation of CIPS/IPS heterostructure and IPS with Cu atoms, 1×2×2 and 2×2×2 Γ-centered k-mesh were used, respectively. All the heterostructures were fully relaxed until the force on each atom is less than 0.01 eV/Å. The lattice parameters of the CIPS/IPS heterostructures were also optimized, since the interlayer distance of a CIPS/IPS heterostructure changes as a function of the Cu/In ratio[23]. The Cu migration barrier was calculated using the climbing nudged elastic band (CI-NEB) method[66, 67]. Three images were interpolated

between initial and final states, and the images were relaxed until the force perpendicular to the path is less than 0.01 eV/Å. The dielectric constant was calculated by the linear response method implemented in VASP[68].

Supporting Information

S1: Correlative PFM and SDM with SMM. S2: SDM full dataset with intermediate temperatures. S3: IDS-PFM of flake in Figure 5. S4: Quantification of the dielectric constant and conductivity. S5: LP-CIPS atomic configurations. S6. Finite element simulations of the CIPS/IPS interface. S7 CIPS and IPS atomic configurations. S8: Construction of a IPS/CIPS/IPS heterostructure. S9: Alternative CIPS/IPS heterostructures. S10: Cu migration in IPS.

Acknowledgements

Experimental research was supported by the Center for Nanophase Materials Sciences, (CNMS), which is a US Department of Energy, Office of Science User Facility at Oak Ridge National Laboratory. Theoretical work at Vanderbilt University (X. J., A. O., S. T. P.) was supported by the U.S. Department of Energy, Office of Science, Basic Energy Sciences, Materials Science and Engineering Division grant No. DE-FG02-09ER46554. This manuscript has been authored by UT-Battelle, LLC, under Contract No. DEAC0500OR22725 with the U.S. Department of Energy. Additional support for sample synthesis and manuscript preparation was supplied by the United States Air Force Office of Scientific Research (AFOSR) LRIR 18RQCOR100 and AOARD-MOST Grant Number F4GGA21207H002. G.G. and R.M-S. acknowledge support from the Spanish Ministerio de Economıa, Industria y Competitividad and EU FEDER through Grant No. PID2019-110210GB-I00.

Author contributions

M.C., and L.C. conceived and designed the research. M.C. carried out all experiments and performed the data analysis. M.A.S and M.A.M prepared the sample. X.J., A.O. and S.T.P performed the DFT calculations. R.M.S and G.G. made the finite-element-calculations used to quantify the SDM. S.N. carried out the SMM measurement. L.C., M.C., S.N. and, P.M. interpreted the results. M.C., X.J., S.T.P and L.C co-wrote the manuscript with input from all the authors.

References

1. Xue, F.; He, J.-H.; Zhang, X., Emerging van der Waals ferroelectrics: Unique properties and novel devices. *Applied Physics Reviews* **2021,** *8* (2), 021316.
2. Liu, F.; You, L.; Seyler, K. L.; Li, X.; Yu, P.; Lin, J.; Wang, X.; Zhou, J.; Wang, H.; He, H.; Pantelides, S. T.; Zhou, W.; Sharma, P.; Xu, X.; Ajayan, P. M.; Wang, J.; Liu, Z., Room-temperature ferroelectricity in CuInP2S6 ultrathin flakes. *Nat Commun* **2016,** *7*, 12357.
3. Qiao, H.; Wang, C.; Choi, W. S.; Park, M. H.; Kim, Y., Ultra-thin ferroelectrics. *Materials Science and Engineering: R: Reports* **2021,** *145*, 100622.
4. Susner, M. A.; Chyasnavichyus, M.; McGuire, M. A.; Ganesh, P.; Maksymovych, P., Metal thio-and selenophosphates as multifunctional van der Waals layered materials. *Advanced Materials* **2017,** *29* (38), 1602852.
5. Yan, X.-Q.; Zhao, X.; Xu, H.; Zhang, L.; Liu, D.; Zhang, Y.; Huo, C.; Liu, F.; Xie, J.; Dong, X., Temperature-tunable optical properties and carrier relaxation of CuInP 2 S 6 crystals under ferroelectric-paraelectric phase transition. *Journal of Materials Chemistry C* **2022,** *10* (2), 696-706.
6. Jiang, X.; Wang, X.; Wang, X.; Zhang, X.; Niu, R.; Deng, J.; Xu, S.; Lun, Y.; Liu, Y.; Xia, T., Manipulation of current rectification in van der Waals ferroionic CuInP2S6. *Nature communications* **2022,** *13* (1), 1-8.
7. Chen, J.; Zhu, C.; Cao, G.; Liu, H.; Bian, R.; Wang, J.; Li, C.; Chen, J.; Fu, Q.; Liu, Q., Mimicking neuroplasticity via ion migration in van der Waals layered copper indium thiophosphate. *Advanced Materials* **2021**, 2104676.
8. Neumayer, S. M.; Zhao, Z.; O'Hara, A.; McGuire, M. A.; Susner, M. A.; Pantelides, S. T.; Maksymovych, P.; Balke, N., Nanoscale Control of Polar Surface Phases in Layered van der Waals CuInP2S6. *ACS nano* **2022**.
9. Maisonneuve, V.; Cajipe, V.; Simon, A.; Von Der Muhll, R.; Ravez, J., Ferrielectric ordering in lamellar CuInP 2 S 6. *Physical Review B* **1997,** *56* (17), 10860.
10. Neumayer, S. M.; Eliseev, E. A.; Susner, M. A.; Tselev, A.; Rodriguez, B. J.; Brehm, J. A.; Pantelides, S. T.; Panchapakesan, G.; Jesse, S.; Kalinin, S. V., Giant negative electrostriction and dielectric tunability in a van der Waals layered ferroelectric. *Physical Review Materials* **2019,** *3* (2), 024401.
11. Brehm, J. A.; Neumayer, S. M.; Tao, L.; O'Hara, A.; Chyasnavichus, M.; Susner, M. A.; McGuire, M. A.; Kalinin, S. V.; Jesse, S.; Ganesh, P., Tunable quadruple-well ferroelectric van der Waals crystals. *Nature Materials* **2020,** *19* (1), 43-48.
12. Neumayer, S. M.; Tao, L.; O'Hara, A.; Brehm, J.; Si, M.; Liao, P.-Y.; Feng, T.; Kalinin, S. V.; Peide, D. Y.; Pantelides, S. T., Alignment of polarization against an electric field in van der Waals ferroelectrics. *Physical Review Applied* **2020,** *13* (6), 064063.
13. Zhang, D.; Luo, Z. D.; Yao, Y.; Schoenherr, P.; Sha, C.; Pan, Y.; Sharma, P.; Alexe, M.; Seidel, J., Anisotropic Ion Migration and Electronic Conduction in van der Waals Ferroelectric CuInP2S6. *Nano Lett* **2021,** *21* (2), 995-1002.
14. Balke, N.; Neumayer, S. M.; Brehm, J. A.; Susner, M. A.; Rodriguez, B. J.; Jesse, S.; Kalinin, S. V.; Pantelides, S. T.; McGuire, M. A.; Maksymovych, P., Locally Controlled Cu-Ion Transport in Layered Ferroelectric CuInP2S6. *ACS Appl Mater Interfaces* **2018,** *10* (32), 27188-27194.

15. Susner, M. A.; Chyasnavichyus, M.; Puretzky, A. A.; He, Q.; Conner, B. S.; Ren, Y.; Cullen, D. A.; Ganesh, P.; Shin, D.; Demir, H., Cation–eutectic transition via sublattice melting in CuInP2S6/In4/3P2S6 van der Waals layered crystals. *ACS nano* **2017,** *11* (7), 7060-7073.
16. Rao, R.; Selhorst, R.; Conner, B. S.; Susner, M. A., Ferrielectric-paraelectric phase transitions in layered CuInP2S6 and CuInP2S6-In4/3P2S6 heterostructures: A Raman spectroscopy and X-ray diffraction study. **2021,** *arXiv, 2111.00615, 31st Oct. 2021,* https://doi.org/10.48550/arXiv.2111.00615.
17. Checa, M.; Ivanov, I.; Neumayer, S. M.; Susner, M. A.; McGuire, M. A.; Maksymovych, P.; Collins, L., Correlative piezoresponse and micro-Raman imaging of CuInP2S6–In4/3P2S6 flakes unravels phase-specific phononic fingerprint via unsupervised learning. *Applied Physics Letters* **2022,** *121* (6), 062901.
18. Li, P.; Chaturvedi, A.; Zhou, H.; Zhang, G.; Li, Q.; Xue, J.; Zhou, Z.; Wang, S.; Zhou, K.; Weng, Y., Electrostatic Coupling in MoS2/CuInP2S6 Ferroelectric vdW Heterostructures. *Advanced Functional Materials* **2022**, 2201359.
19. Li, Y.; Fu, J.; Mao, X.; Chen, C.; Liu, H.; Gong, M.; Zeng, H., Enhanced bulk photovoltaic effect in two-dimensional ferroelectric CuInP2S6. *Nature communications* **2021,** *12* (1), 1-7.
20. Jin, H.; Guo, C.; Liu, X.; Liu, J.; Vasileff, A.; Jiao, Y.; Zheng, Y.; Qiao, S.-Z., Emerging two-dimensional nanomaterials for electrocatalysis. *Chemical reviews* **2018,** *118* (13), 6337-6408.
21. Collins, L.; Liu, Y.; Ovchinnikova, O. S.; Proksch, R., Quantitative Electromechanical Atomic Force Microscopy. *ACS Nano* **2019,** *13* (7), 8055-8066.
22. Wojdeł, J. C.; Iniguez, J., Ferroelectric transitions at ferroelectric domain walls found from first principles. *Physical Review Letters* **2014,** *112* (24), 247603.
23. Susner, M. A.; Belianinov, A.; Borisevich, A.; He, Q.; Chyasnavichyus, M.; Demir, H.; Sholl, D. S.; Ganesh, P.; Abernathy, D. L.; McGuire, M. A., High-T c layered ferrielectric crystals by coherent spinodal decomposition. *ACS nano* **2015,** *9* (12), 12365-12373.
24. Vasudevan, R. K.; Neumayer, S. M.; Susner, M. A.; McGuire, M. A.; Pantelides, S. T.; Maksymovych, P.; Leonard, D. N.; Balke, N.; Borisevich, A. Y., Domains and Topological Defects in Layered Ferrielectric Materials: Implications for Nanoelectronics. *ACS Applied Nano Materials* **2020,** *3* (8), 8161-8166.
25. Labuda, A.; Proksch, R., Quantitative measurements of electromechanical response with a combined optical beam and interferometric atomic force microscope. *Applied Physics Letters* **2015,** *106* (25), 253103.
26. Novoselov, K. S.; Geim, A. K.; Morozov, S. V.; Jiang, D.-e.; Zhang, Y.; Dubonos, S. V.; Grigorieva, I. V.; Firsov, A. A., Electric field effect in atomically thin carbon films. *science* **2004,** *306* (5696), 666-669.
27. Neumayer, S. M.; Brehm, J. A.; Tao, L.; O'Hara, A.; Ganesh, P.; Jesse, S.; Susner, M. A.; McGuire, M. A.; Pantelides, S. T.; Maksymovych, P., Local Strain and Polarization Mapping in Ferrielectric Materials. *ACS Applied Materials & Interfaces* **2020,** *12* (34), 38546-38553.
28. Chyasnavichyus, M.; Susner, M. A.; Ievlev, A. V.; Eliseev, E. A.; Kalinin, S. V.; Balke, N.; Morozovska, A. N.; McGuire, M. A.; Maksymovych, P., Size-effect in layered ferrielectric CuInP2S6. *Applied Physics Letters* **2016,** *109* (17), 172901.
29. Jesse, S.; Kumar, A.; Arruda, T. M.; Kim, Y.; Kalinin, S. V.; Ciucci, F., Electrochemical strain microscopy: Probing ionic and electrochemical phenomena in solids at the nanometer level. *MRS bulletin* **2012,** *37* (7), 651-658.

30. Balke, N.; Jesse, S.; Morozovska, A.; Eliseev, E.; Chung, D.; Kim, Y.; Adamczyk, L.; Garcia, R.; Dudney, N.; Kalinin, S., Nanoscale mapping of ion diffusion in a lithium-ion battery cathode. *Nature nanotechnology* **2010,** *5* (10), 749-754.
31. Ma, R. R.; Xu, D. D.; Zhong, Q. L.; Zhong, C. R.; Huang, R.; Xiang, P. H.; Zhong, N.; Duan, C. G., Nanoscale Mapping of Cu-Ion Transport in van der Waals Layered CuCrP2S6. *Advanced Materials Interfaces* **2022,** *9* (4), 2101769.
32. Balke, N.; Neumayer, S. M.; Brehm, J. A.; Susner, M. A.; Rodriguez, B. J.; Jesse, S.; Kalinin, S. V.; Pantelides, S. T.; McGuire, M. A.; Maksymovych, P., Locally controlled Cu-ion transport in layered ferroelectric CuInP2S6. *ACS applied materials & interfaces* **2018,** *10* (32), 27188-27194.
33. Badur, S.; Renz, D.; Cronau, M.; Göddenhenrich, T.; Dietzel, D.; Roling, B.; Schirmeisen, A., Characterization of Vegard strain related to exceptionally fast Cu-chemical diffusion in Cu2Mo6S8 by an advanced electrochemical strain microscopy method. *Scientific reports* **2021,** *11* (1), 1-8.
34. Vasudevan, R. K.; Balke, N.; Maksymovych, P.; Jesse, S.; Kalinin, S. V., Ferroelectric or non-ferroelectric: Why so many materials exhibit "ferroelectricity" on the nanoscale. *Applied Physics Reviews* **2017,** *4* (2), 021302.
35. Checa, M.; Neumayer, S.; Susner, M. A.; McGuire, M. A.; Maksymovych, P.; Collins, L., Simultaneous mapping of nanoscale dielectric, electrochemical, and ferroelectric surface properties of van der Waals layered ferroelectric via advanced SPM. *Applied Physics Letters* **2021,** *119* (25), 252905.
36. Banys, J.; Macutkevic, J.; Samulionis, V.; Brilingas, A.; Vysochanskii, Y., Dielectric and ultrasonic investigation of phase transition in CuInP2S6 crystals. *Phase Transitions* **2004,** *77* (4), 345-358.
37. Zhou, S.; You, L.; Chaturvedi, A.; Morris, S. A.; Herrin, J. S.; Zhang, N.; Abdelsamie, A.; Hu, Y.; Chen, J.; Zhou, Y., Anomalous polarization switching and permanent retention in a ferroelectric ionic conductor. *Materials Horizons* **2020,** *7* (1), 263-274.
38. Fumagalli, L.; Gomila, G., Probing dielectric constant at the nanoscale with scanning probe microscopy. In *Capacitance Spectroscopy of Semiconductors*, Pan Stanford Publishing: Oxfordshire, **2018**.
39. Zhang, D.; Luo, Z.-D.; Yao, Y.; Schoenherr, P.; Sha, C.; Pan, Y.; Sharma, P.; Alexe, M.; Seidel, J., Anisotropic Ion Migration and Electronic Conduction in van der Waals Ferroelectric CuInP2S6. *Nano letters* **2021,** *21* (2), 995-1002.
40. Checa, M.; Millan-Solsona, R.; Mares, A. G.; Pujals, S.; Gomila, G., Fast Label-Free Nanoscale Composition Mapping of Eukaryotic Cells Via Scanning Dielectric Force Volume Microscopy and Machine Learning. *Small Methods* **2021,** *5* (7), 2100279.
41. Balakrishnan, H.; Millan-Solsona, R.; Checa, M.; Fabregas, R.; Fumagalli, L.; Gomila, G., Depth mapping of metallic nanowire polymer nanocomposites by scanning dielectric microscopy. *Nanoscale* **2021,** *13* (22), 10116-10126.
42. Fumagalli, L.; Esteban-Ferrer, D.; Cuervo, A.; Carrascosa, J. L.; Gomila, G., Label-free identification of single dielectric nanoparticles and viruses with ultraweak polarization forces. *Nature materials* **2012,** *11* (9), 808-816.
43. Kyndiah, A.; Checa, M.; Leonardi, F.; Millan-Solsona, R.; Di Muzio, M.; Tanwar, S.; Fumagalli, L.; Mas-Torrent, M.; Gomila, G., Nanoscale Mapping of the Conductivity and Interfacial Capacitance of an Electrolyte-Gated Organic Field-Effect Transistor under Operation. *Advanced Functional Materials* **2021,** *31* (5), 2008032.

44. Millan-Solsona, R.; Checa, M.; Fumagalli, L.; Gomila, G., Mapping the capacitance of self-assembled monolayers at metal/electrolyte interfaces at the nanoscale by in-liquid scanning dielectric microscopy. *Nanoscale* **2020,** *12* (40), 20658-20668.
45. Checa, M.; Millan-Solsona, R.; Glinkowska Mares, A.; Pujals, S.; Gomila, G., Dielectric Imaging of Fixed HeLa Cells by In-Liquid Scanning Dielectric Force Volume Microscopy. *Nanomaterials* **2021,** *11* (6), 1402.
46. Gomila, G.; Gramse, G.; Fumagalli, L., Finite-size effects and analytical modeling of electrostatic force microscopy applied to dielectric films. *Nanotechnology* **2014,** *25* (25), 255702.
47. Checa, M.; Neumayer, S. M.; Tsai, W.-Y.; Collins, L., Advanced Modes of Electrostatic and Kelvin Probe Force Microscopy for Energy Applications. In *Atomic Force Microscopy for Energy Research*, CRC Press; Oxfordshire, **2022**; pp 45-104.
48. Trainer, M., Ferroelectrics and the Curie-Weiss law. *European Journal of Physics* **2000,** *21* (5), 459.
49. Giordano, N. J.; De Jong, M. L.; McKay, S. R.; Christian, W., Computational physics. *Computers in Physics* **1997,** *11* (4), 351-351.
50. Belianinov, A.; He, Q.; Dziaugys, A.; Maksymovych, P.; Eliseev, E.; Borisevich, A.; Morozovska, A.; Banys, J.; Vysochanskii, Y.; Kalinin, S. V., CuInP(2)S(6) Room Temperature Layered Ferroelectric. *Nano Lett* **2015,** *15* (6), 3808-14.
51. O'Hara, A.; Balke, N.; Pantelides, S. T., Unique features of polarization in ferroelectric ionic conductors. *Advanced Electronic Materials* **2022,** *8* (3), 2100810.
52. Wojdeł, J. C.; Hermet, P.; Ljungberg, M. P.; Ghosez, P.; Iniguez, J., First-principles model potentials for lattice-dynamical studies: general methodology and example of application to ferroic perovskite oxides. *Journal of Physics: Condensed Matter* **2013,** *25* (30), 305401.
53. Ares, P.; Cea, T.; Holwill, M.; Wang, Y. B.; Roldán, R.; Guinea, F.; Andreeva, D. V.; Fumagalli, L.; Novoselov, K. S.; Woods, C. R., Piezoelectricity in monolayer hexagonal boron nitride. *Advanced Materials* **2020,** *32* (1), 1905504.
54. Weston, A.; Castanon, E. G.; Enaldiev, V.; Ferreira, F.; Bhattacharjee, S.; Xu, S.; Corte-León, H.; Wu, Z.; Clark, N.; Summerfield, A., Interfacial ferroelectricity in marginally twisted 2D semiconductors. *Nature Nanotechnology* **2022**, 1-6.
55. Xu, D.-D.; Ma, R.-R.; Zhao, Y.-F.; Guan, Z.; Zhong, Q.-L.; Huang, R.; Xiang, P.-H.; Zhong, N.; Duan, C.-G., Unconventional out-of-plane domain inversion via in-plane ionic migration in a van der Waals ferroelectric. *Journal of Materials Chemistry C* **2020,** *8* (21), 6966-6971.
56. Boschker, H. T.; Cook, P. L.; Polerecky, L.; Eachambadi, R. T.; Lozano, H.; Hidalgo-Martinez, S.; Khalenkow, D.; Spampinato, V.; Claes, N.; Kundu, P., Efficient long-range conduction in cable bacteria through nickel protein wires. *Nature communications* **2021,** *12* (1), 1-12.
57. Kresse, G.; Hafner, J., Ab initio molecular dynamics for liquid metals. *Physical review B* **1993,** *47* (1), 558.
58. Kresse, G.; Hafner, J., Ab initio molecular dynamics for open-shell transition metals. *Physical Review B* **1993,** *48* (17), 13115.
59. Kresse, G.; Furthmüller, J., Efficiency of ab-initio total energy calculations for metals and semiconductors using a plane-wave basis set. *Computational materials science* **1996,** *6* (1), 15-50.
60. Kresse, G.; Joubert, D., From ultrasoft pseudopotentials to the projector augmented-wave method. *Physical review b* **1999,** *59* (3), 1758.

61. Blöchl, P. E., Projector augmented-wave method. *Physical Review B* **1994,** *50* (24), 17953-17979.
62. Perdew, J. P.; Burke, K.; Ernzerhof, M., Generalized gradient approximation made simple. *Physical review letters* **1996,** *77* (18), 3865.
63. Grimme, S., Semiempirical GGA-type density functional constructed with a long-range dispersion correction. *Journal of computational chemistry* **2006,** *27* (15), 1787-1799.
64. Grimme, S.; Antony, J.; Ehrlich, S.; Krieg, H., A consistent and accurate ab initio parametrization of density functional dispersion correction (DFT-D) for the 94 elements H-Pu. *The Journal of chemical physics* **2010,** *132* (15), 154104.
65. Grimme, S.; Ehrlich, S.; Goerigk, L., Effect of the damping function in dispersion corrected density functional theory. *Journal of computational chemistry* **2011,** *32* (7), 1456-1465.
66. Henkelman, G.; Jónsson, H., Improved tangent estimate in the nudged elastic band method for finding minimum energy paths and saddle points. *The Journal of chemical physics* **2000,** *113* (22), 9978-9985.
67. Henkelman, G.; Uberuaga, B. P.; Jónsson, H., A climbing image nudged elastic band method for finding saddle points and minimum energy paths. *The Journal of chemical physics* **2000,** *113* (22), 9901-9904.
68. Gajdoš, M.; Hummer, K.; Kresse, G.; Furthmüller, J.; Bechstedt, F., Linear optical properties in the projector-augmented wave methodology. *Physical Review B* **2006,** *73* (4), 045112.